



P-doped tubular g-C₃N₄ with surface carbon defects: Universal synthesis and enhanced visible-light photocatalytic hydrogen production

Shien Guo^{a,b,1}, Yunqi Tang^{a,1}, Ying Xie^a, Chungui Tian^a, Qingmao Feng^a, Wei Zhou^a, Baojiang Jiang^{a,*}

^a Key Laboratory of Functional Inorganic Material Chemistry, Ministry of Education of PR China, Heilongjiang University, Harbin, PR China

^b Institute of Chemistry, Chinese Academy of Sciences, PR China

ARTICLE INFO

Article history:

Received 19 April 2017

Received in revised form 5 July 2017

Accepted 9 July 2017

Available online 11 July 2017

Keywords:

P-doped tubular g-C₃N₄

Photocatalyst

Hydrogen evolution

Carbon defects

Density functional theory

ABSTRACT

Hetero-element doping or vacancy defects of g-C₃N₄ framework were found significantly to control its electronic structure and enhance photocatalytic activity under visible light. Herein, we fabricated P-doped tubular g-C₃N₄ (P-TCN) with surface carbon defects wherein the P-doping and carbon defects were conveniently introduced during thermal polymerization of a supramolecular precursor. The supramolecular precursor of rod-like morphology was obtained only from melamine molecules under a sodium pyrophosphate-assisted hydrothermal process. As contrast, similar P-doped g-C₃N₄ tubes were obtained using other phosphates, such as ammonium phosphate, sodium hypophosphite and sodium phosphite, thus highlighting the versatility of this method to tune the morphology and C/N ratio for g-C₃N₄ tubes. The photocatalytic activities of P-TCNs were evaluated using hydrogen evolution from water under visible light. Among these, P-TCN obtained by sodium pyrophosphate-assisted hydrothermal reaction showed the highest photocatalytic activity due to high P element doping, enhanced visible light absorption and improved charge separation. The novel synthetic method described here thus represents an effective way of non-metal doping and C/N ratio tuning of g-C₃N₄ with excellent photocatalytic performance.

© 2017 Elsevier B.V. All rights reserved.

1. Introduction

Hydrogen production, employing a photocatalyst and solar energy, is attracting great interest in regard to global energy and environmental issues [1–5]. One of the primary challenges in practical application of this technique is to design a robust, cheap and stable photocatalyst that exhibits excellent visible-light photocatalytic activity, as shown recently with the focus on graphitic carbon nitride (g-C₃N₄) [6–8]. As a new member of photocatalyst for photocatalytic hydrogen evolution, this cheap, easily available organic semiconductor shows great promise in photocatalytic hydrogen evolution, heterogeneous organocatalysis and environmental protection [9,10]. However, g-C₃N₄ suffers from a number of disadvantages, such as low visible-light utilization efficiency, high electron-hole recombination rate and low surface area [11–13]. To improve the hydrogen evolution activity of g-C₃N₄,

novel synthesis strategies have emerged, which include controlling the design of macro-nanostructures and hetero-element doping, such as using P, S, and B for g-C₃N₄ [14–16], to effectively change the electronic structure of g-C₃N₄ as well as their surface properties, thus improving photocatalytic performance [17,18]. Meanwhile, the special point defects are important to enhance the photocatalytic reaction activity because these defects can modify the electronic structure and act as specific sites for reactant molecules in the photocatalytic process [19]. For g-C₃N₄, the intrinsic point defects, such as carbon or nitrogen vacancies, have exhibited interesting experimental phenomena [20,21]. However, for photocatalytic hydrogen production, some defects in the inner bulk material may serve as recombination centres for photo-generated electrons or holes, while surface defects can effectively promote charge separation or facilitate charge transfer [22].

In addition, the supramolecular precursor by hydrogen bonding is an effective way to construct stable macro-nanostructure g-C₃N₄ [23,24]. The hydrogen bonding has a strong directional component, which contributes to the design of g-C₃N₄ with unique structure and morphology [25,26]. Of particular interest is that the supramolecular assembly is expected to yield preformed micro-

* Corresponding author.

E-mail address: jiangbaojiang88@sina.com (B. Jiang).

¹ These authors contributed equally to the work.

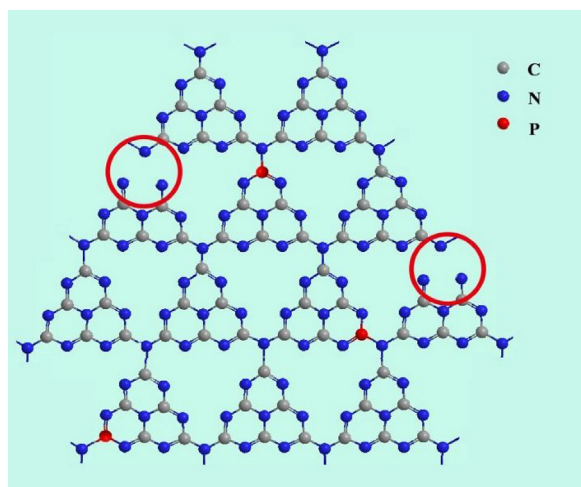


Fig. 1. Schematic structure of P-doped g-C₃N₄ with surface carbon defects.

or nanostructures depending on the precursor molecules, solvent type, and synthesis temperatures, which may be incorporated into g-C₃N₄. For example, melamine and cyanuric acid or derivatives have been described for assembly into the supramolecular precursor structure for the formation of g-C₃N₄ [27]. Recently, we have reported on phosphorus-doped hexagonal tubular g-C₃N₄ with a layered stacking structure from melamine precursor [14]. Hexagonal g-C₃N₄ possesses excellent visible-light photocatalytic performance for hydrogen evolution due to its narrow band gap structure and enhanced electrical conductivity.

In the last few years, many researchers had accomplished to modulate graphitic carbon nitride by phosphorus doping [28–32]. According to the previous work [33], the existence of phosphorus in the structure of graphitic carbon nitride can decrease the band gap energy, increase the separation efficiency of photogenerated electrons and holes and extend the light response of graphitic carbon nitride, simultaneously. However, in this work, the phosphorus-doped tubular P-TCN with surface carbon defects is produced from a supramolecular precursor under sodium pyrophosphate-assisted hydrothermal process. In like manner, a series of phosphorus-containing compounds, including ammonium phosphate, sodium hypophosphite and sodium phosphite, are employed to fabricate the supramolecular precursor, resulting in a similar-formed P-TCN. A possible schematic structure of P-doped g-C₃N₄ with surface carbon defects is shown in Fig. 1. The P-TCN products with different C/N ratios exhibit excellent photocatalytic activities for hydrogen evolution under visible light. Our study develops a universal strategy to construct a special structural g-C₃N₄ with adjustable C/N ratio and heterogeneous element doping for photocatalytic applications.

2. Experimental

2.1. Preparation of phosphorus-doped tubular P-TCN with surface carbon defects

First, 1.26 g (10 mmol) melamine is dissolved in 100 mL deionized water under a water bath at 85 °C, then different amounts of sodium pyrophosphate were added into the solution with strong stirring for 30 min. Subsequently the mixture was transferred into an autoclave with Teflon liner and heated at 180 °C for 10 h. The mixture was centrifuged, washed with deionized water and dried in an oven at 60 °C. Finally, the resultant solids were heated at 500 °C for 4 h under a flow of nitrogen at a heating rate of 2.5 °C/min. The sodium pyrophosphate modified samples were defined as CN-SP.

Similarly, a series of phosphorus-containing compounds, including ammonium phosphate, sodium hypophosphite and sodium phosphite, were employed to react with melamine, and the corresponding calcination products were denoted as CN-AP, CN-SH, CN-SPh.

For comparison, g-C₃N₄ was also prepared with melamine placed in a porcelain crucible and calcined at 550 °C for 4 h in N₂ atmosphere at a heating rate of 2.5 °C/min, and then the product was ground to a homogeneous powder.

2.2. Characterization

X-ray powder diffraction (XRD) patterns were obtained by Bruker D8. Scanning electron microscopy (SEM) micrographs were taken using a Hitachi S-4800 instrument operating at 15 kV. Transmission electron microscopy (TEM) was performed on a JEM-2100 electron microscope (JEOL, Japan) with an acceleration voltage of 200 kV. Fourier transform infrared spectroscopy (FT-IR) was recorded on a Perkin-Elmer Spectrum One spectrometer using KBr pellets. Photoluminescence spectra (PL) were recorded with a Hitachi F-4600 fluorescence spectrophotometer at room temperature. The specific surface area was determined according to the Brunauer-Emmett-Teller (BET) method using a Tristar II 3020 surface area and porosity analyzer (micromeritics). UV–vis absorption spectroscopy was recorded using a UV–vis spectrophotometer (Shimadzu UV-2550). X-ray photoelectron spectroscopy (XPS) analysis was performed on a VG ESCALAB MK II with an Mg K α (1253.6 eV) achromatic X-ray source. The thermal stability of the as-prepared samples was verified using a thermogravimetric analyzer (SDT Q600).

2.3. Photocatalytic hydrogen production

The photocatalytic hydrogen production experiment was conducted in an on-line photocatalytic hydrogen production system (AuLight, Beijing, CEL-SPH₂N) at an ambient temperature of 20 °C. 0.1 g catalyst was suspended in a mixture of 80 mL distilled water and 20 mL methanol in the reaction cell with magnetic stirring. 1 wt.% Pt loaded photocatalysts were prepared by a known standard in-situ photo-deposition method using H₂PtCl₆ aqueous solution. A Xenon 300 W lamp (Oriel, USA) equipped with a 420-nm cut-off filter was used as the light irradiation source. Gas evolution was observed only under irradiation, being analyzed by an on-line gas chromatograph (SP7800, TCD, molecular sieve 5 Å, N₂ carrier, Beijing Keruida Limited). Once the photocatalytic reaction of a testing cycle of 3 h was completed, the reactor was replenished with 1 mL of methanol and degassed in a vacuum before starting the subsequent cycle.

2.4. Photoelectrochemical characterization

Electrochemical measurements were conducted with a BAS Epsilon Electrochemical System in a conventional three-electrode cell, using a Pt plate as the counter electrode and a saturated calomel electrode as the reference electrode. The working electrode was prepared by spreading aqueous slurries of as-synthesised samples (50 μ L) over FTO glass substrate. The suspension was prepared by dispersing samples (20 mg) with Nafion solution in ethanol (1 wt.%, 2 mL). The electrodes were then dried in an oven, and calcined at 400 °C for 30 min under a flow of N₂ gas. The working electrode was irradiated from its reverse side. The supporting electrolyte was an aqueous solution of Na₂SO₄ (0.2 M) and purged with nitrogen for 1 h before measurement.

2.5. Density-functional-theory (DFT) calculations

The density of states (DOSs) of g-C₃N₄ and P-doped g-C₃N₄ were calculated by using the CASTEP code. To deal with the exchange-correlation energy, Perdew-Burke-Ernzerhof (PBE) functional form with a generalized gradient approximation (GGA-PBE) was adopted. Furthermore, a scissor operator contributing about 1.226 eV was introduced to correct the well-known band gap problem. To avoid the pseudo-interactions between periodic images along z axis, a vacuum region with a length of 15 Å was introduced into the 2D slabs, as shown in Fig. 7(a). The lattice constants for the (2 × 2 × 1) hexagonal supercell were optimized to be *a* = 16.7 Å and *b* = 12.4 Å, respectively. With the application of Ultrasoft pseudo-potential, the plane wave cut-off was determined to be 340 eV, and the sampling over the Brillouin zone was treated by a (3 × 3 × 4) supercell. This set of parameters guarantees that the energy tolerance is within 1.0 × 10^{−5} eV per atom.

3. Results and discussion

The supramolecular precursors were obtained under a diverse phosphate-assisted hydrothermal process. Scanning electron microscopy (SEM) was selected to observe the surface morphology and structure (Fig. 2). As shown in SEM images (Fig. 2a, c, e, g), all supramolecular precursors possess a similar rod-like structure. There are two main reactions for the formation of supramolecular precursors: I) Table S1 shows that the pH of the reaction system is higher than 7. During the hydrothermal process, the melamine is partially hydrolyzed to cyanuric acid under alkaline conditions [34]. II) Through the self-assembly of melamine with in situ formed cyanuric acid, the supramolecular rod structure is obtained, similar to our previous work. Following thermal polymerization, a typical tubular structure of g-C₃N₄ is obtained. However, for the precursors of CN-AP, CN-SH, and CN-SPh, most of them show a typical tetragonal structure. Actually, the precursor of CN-SP, using sodium pyrophosphate, displays a hexagonal rod structure with a diameter of 10–20 μm (Fig. 2e). As a result, the calcination product CN-SP shows clear hexagonal and tubular morphology, which is different from other products, such as CN-AP, CN-SH, and CN-SPh, possibly due to a different molecular configuration of the supramolecular precursor with a different phosphate molecule.

The high-magnification SEM image in Fig. 1h further displays that the wall of the hexagonal tube is stacked by nanosheets. The hierarchical structures are homogeneously dispersed onto the surface of nanosheets. Such interesting hierarchical structures offer a large surface area for accommodating active sites, promoting the easy diffusion of reactant and product molecules, as well as enhancing light harvesting. In comparison, bulk g-C₃N₄ obtained directly from melamine shows a morphology of solid agglomerates of several micrometers in size (Fig. S1), which proves that phosphate plays a vital role in the construction of such regular tube morphology.

Representative X-ray diffraction (XRD) patterns of the bulk g-C₃N₄ and the products obtained are shown in Fig. 3A. Bulk g-C₃N₄ gives two typical diffraction peaks at around 13.1° and 27.2° as reported previously, which are respectively due to the in-plane structural packing motif (100) and periodic stacking (002) of layers along the *c*-axis [35]. These two sharp peaks significantly decrease in the final samples pattern (b, c, d, and e), and only a very broad and weak peak appears near 27.2°, suggesting the enhancement of layer space along the *c*-axis for all samples. It is noted that the peak at 13.1° almost disappears due to the hollow in-plane structure of products obtained or to hetero-element doping. Furthermore, during the poly-condensation of the supramolecular precursor, a partial loss of lattice C or N leads to a change in the local crys-

talline structure as well as a decrease in crystalline ordering. In addition, we have explored the effect of calcination temperature, and the characterization result (Figs. S2 and S3) indicate that the melon structure can be obtained at lower temperature (400 °C), but the degree of polymerization is incomplete [36]. However, the relatively complete structure can be obtained at 500 °C.

The interior molecular structures of products were further characterized by Fourier Transform Infrared (FT-IR) spectrometer, which was sensitive to the local structure of materials. The FT-IR spectra of g-C₃N₄ and series of products in Fig. 3B suggest a stable conjugated structure of the CN skeleton. A pronounced absorption at 1200–1600 cm^{−1} is attributed to the stretching vibration of CN heterocyclic [37]; whereas, the sharp peak at 802 cm^{−1} is always recognized as the typical breathing vibration of triazine units, which signifies a complete skeleton g-structure of g-C₃N₄ [38]. The broad band located at 2900–3300 cm^{−1} is related to residual N–H components and O–H bands, associated with uncondensed amino groups and surface-adsorbed H₂O molecules [39]. In comparison with g-C₃N₄, the vibrations of tubular samples are less intensive, especially for the broad band at 2900–3300 cm^{−1}. In this investigation, no P-related group is observed, which is attributed to the low phosphorus content or to the overlapping of the vibration by that of the C–N bond. Moreover, the elemental composition of supramolecular precursors was analyzed by XPS, the results of which are listed in Table S2. The precursors are composed of C, N, O and P elements. The presence of P is most likely from the adsorption of P-containing species onto the supramolecular precursor, which is consistent with previous results.

The unique tubular structure of g-C₃N₄ motivated us to further study its BET surface area and pore structure. Thus, the N₂ sorption isotherms of all products, including g-C₃N₄ bulk, CN-SH, CN-SPh, CN-AP and CN-SP, were investigated and shown in Fig. S4. For Fig. S4a, all samples exhibit type IV isotherms, suggesting well-defined hierarchical pore structure, derived from a hollow tube structure and tube wall with varied and numerous mesoporous and macropores, in agreement with the SEM results. From Table 1, CN-SH, CN-SPh, CN-AP, and CN-SP present large BET surface areas (24.5 m² g^{−1}, 21.8 m² g^{−1}, 32.4 m² g^{−1}, and 28.2 m² g^{−1}, respectively), higher than that of g-C₃N₄ bulk (8.6 m² g^{−1}). Furthermore, Fig. S4b shows quantitative details on pore diameter of all samples. CN-SPh and CN-AP exhibit a wide pore size distribution in the 10–150 nm region, due to a random pore formation induced by gas emission during the thermal polymerization. However, CN-SP mostly exhibits mesoporous of 10–40 nm pore size distribution. These data are in good agreement with the morphology analysis of these samples; therefore, we conclude that a tubular structure of g-C₃N₄, richly endowed with a hierarchical pore structure obtained from supramolecular precursors, is beneficial for increasing the number of activity sites for photocatalytic reaction.

Through the thermal treatment process, supramolecular precursors transformed into tubular products which were further characterized by XPS to reveal their chemical state and elemental composition. The pristine g-C₃N₄ bulk was also selected as reference. From the C1s spectrum (Fig. 4A) for the g-C₃N₄ bulk, the mainly carbon species centering at 284.6 eV and 288.2 eV are assigned to graphitic carbon (C–C) and sp²-hybridized carbon in the N-containing aromatic ring (N–C=N), respectively [40]. However, for CN-SH, CN-SPh, CN-AP and CN-SP samples, the binding energy of N–C=N feature decreases to 288 eV, indicating a slight increase in the electron density which is possibly partly due to P instead of carbon atomics or partly due to carbon defects. For the N1s spectrum in Fig. 4B, a small peak located at 404.2 eV is attributed to the positive charge localization in the heterocycles; the bigger one starting from 396.4 eV to 402.7 eV can be deconvoluted into three peaks, including 398.4 eV for sp²-hybridized nitrogen in triazine rings C–N=C (N_{2c}), 400.0 eV for tertiary nitro-

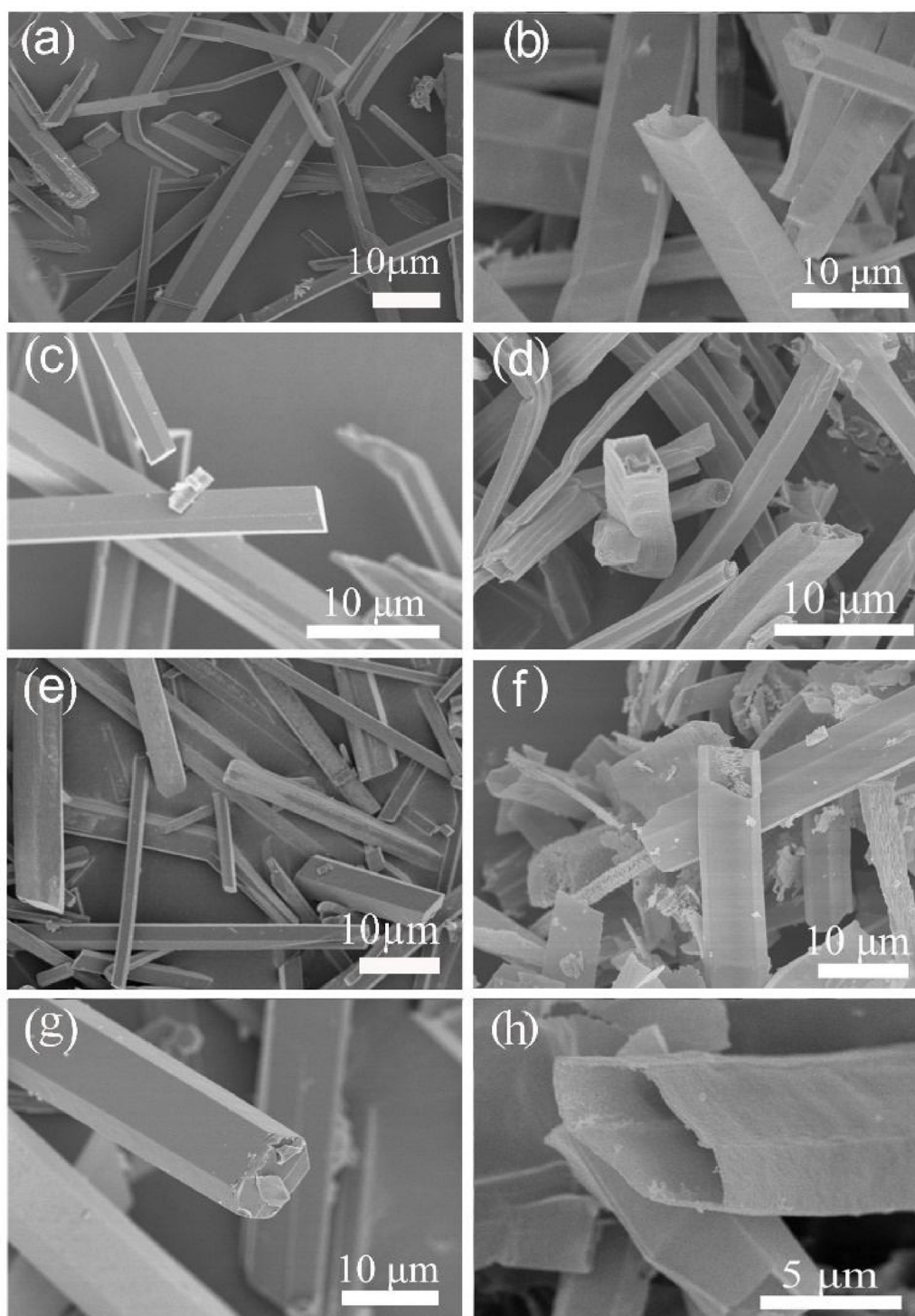


Fig. 2. SEM images of supramolecular precursor obtained by hydrothermal process at 180 °C for 10 h including (a) CN-SH precursor (using sodium hypophosphite), (c) CN-SPh precursor (using sodium phosphite), (e) CN-AP precursor (using ammonium phosphate), and (g) CN-SP precursor (using sodium pyrophosphate). SEM images of thermal polymerization products including (b) CN-SH, (d) CN-SPh, (f) CN-AP and (h) CN-SP, respectively.

Table 1

BET surface areas and element ratios of resulting g-C₃N₄ bulk, CN-SH, CN-SPh, CN-AP and CN-SP samples. The surface C/N atomic ratios are obtained based on the XPS data, and the bulk C/N mass ratios are from the Element Analyzer.

Catalyst	Surface area/m ² g ⁻¹	Surface C/N atomic ratio	Bulk C/N mass ratio	P cont. [wt.%]
g-C ₃ N ₄ bulk	8.6	0.74	0.68	0
CN-SH	24.5	0.72	0.68	0.64
CN-SPh	21.8	0.71	0.68	0.32
CN-AP	32.4	0.70	0.68	0.68
CN-SP	28.2	0.69	0.68	0.87

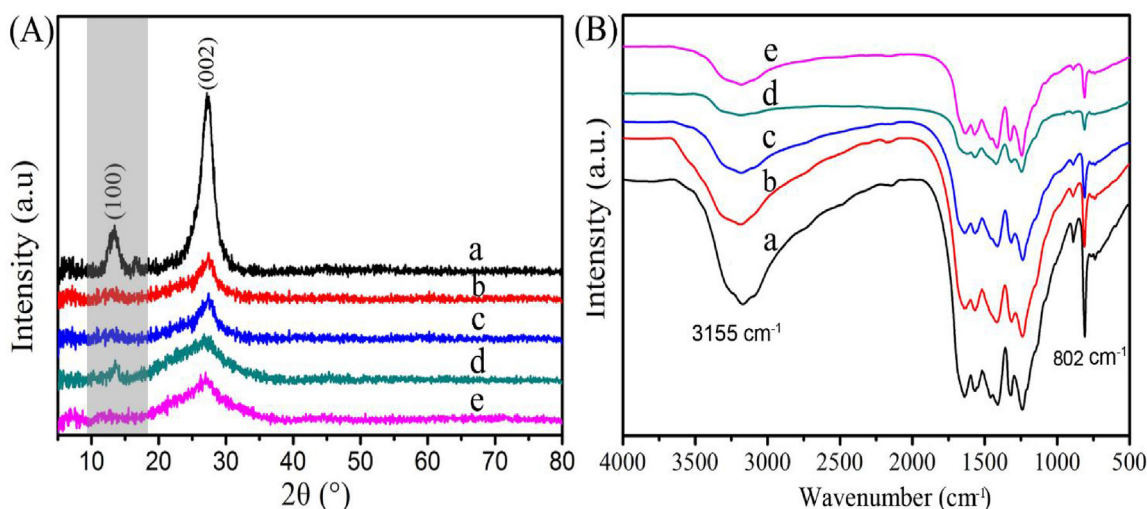


Fig. 3. (A) XRD patterns and (B) FT-IR spectra of synthesized (a) bulk g-C₃N₄, (b) CN-SH, (c) CN-SPh, (d) CN-AP and (e) CN-SP samples.

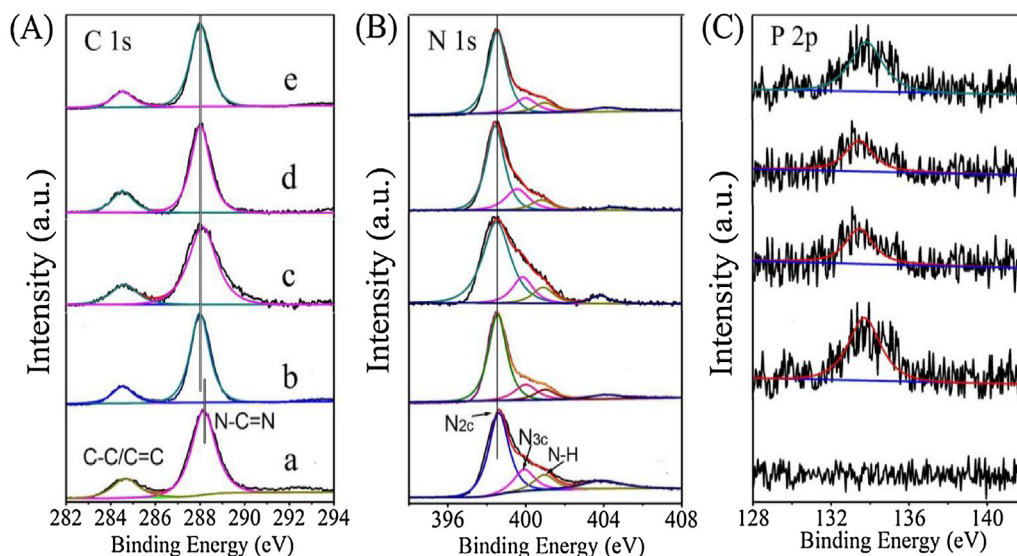


Fig. 4. XPS survey of the synthesized (a) g-C₃N₄ bulk, (b) CN-SH, (c) CN-SPh, (d) CN-AP and (e) CN-SP samples, corresponding to high-resolution spectra of (A) C1s, (B) N1s and (C) P 2p, respectively.

gen N-(C)₃ groups (N_{3c}) and 401.2 eV for amino groups carrying hydrogen (C-N-H) [41]. A careful examination reveals that the surface atom ratio of carbon to nitrogen (C/N) of different samples changes a lot (Table 1), especially for CN-SP. For g-C₃N₄ bulk, the ratio C/N is 0.74. But for CN-AP, CN-SPh, CN-SH, and CN-SP, the ratios of C/N are 0.70, 0.71, 0.72, and 0.69, respectively, which imply an introduction of defects such as carbon into g-C₃N₄ during synthesis. In addition, a change occurs in electron structure and energy band structure of g-C₃N₄. Meanwhile, the peak of P 2p binding energy in the XPS spectra (Fig. 3C) is centered at 133.5 eV, which is typical for P-N coordination [42], indicating that P most probably replaces C in the triazine rings to form P-N bonds during thermal polymerization. The P ratios of P-doped g-C₃N₄ samples are confirmed by XPS analysis, including CN-SH (0.64 wt.%), CN-SPh (0.32 wt.%), CN-AP (0.68 wt.%), and CN-SP (0.87 wt.%). CN-SP possesses the highest P ratio which is most likely due to a strong interaction between the supramolecular precursor and sodium pyrophosphate. However, XPS technology can only probe surface elements; therefore, the total element ratio of g-C₃N₄ bulk material should be confirmed by the Elemental Ana-

lyzer, the results of which are shown in Table 1. It is interesting to note that the C/N mass ratio within bulk g-C₃N₄ for all samples shows the same value ~0.68, which indicates that carbon defects, only existing on the surface of g-C₃N₄, contribute to the changes in electronic structure; in contrast, the bulk phase structure still remains in the mode of full heptazine rings.

The optical features and electronic band gaps of a series of samples obtained from different precursors were also examined, together with g-C₃N₄ bulk as a reference. And we show the optical photos both of supramolecular precursors and samples in Figs. S5 and S6. As shown in Fig. 5A, a typical absorption band at the 440–450 nm region is observed for the g-C₃N₄ bulk. For P-doped samples, the obvious red shifts of absorption band are observed relative to g-C₃N₄ bulk, indicating P doping and a C defect which can tune the optical property of synthesized g-C₃N₄. From the transformed Kubelka-Munk function [43], the direct band gaps of the samples decrease from 2.75 eV of g-C₃N₄ bulk to 2.63 eV of CN-AP, respectively. The changes are consistent with a previous report that the conjugated polymer doped with heterogeneous elements tends to decrease band gap. In fact, the formation of tube structure also

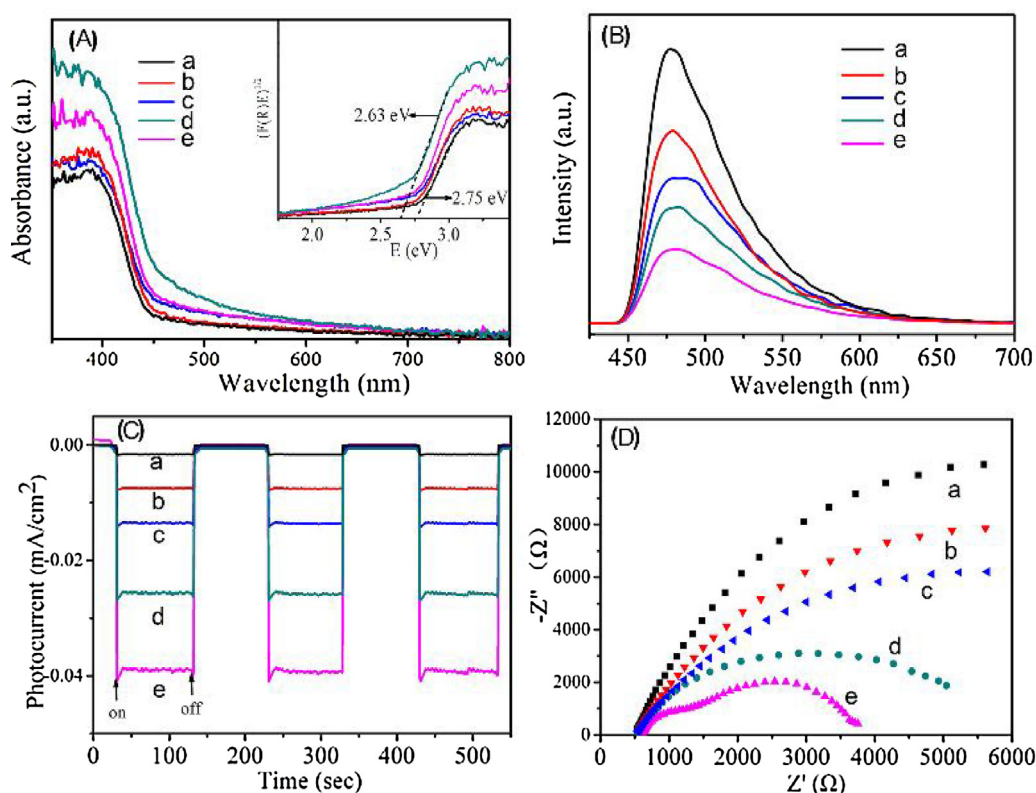


Fig. 5. (A) UV-vis diffuse reflectance spectra and inset is band energy spectra; (B) Photoluminescence emission spectra; (C) Photo-electrochemical properties: the photocurrent responses, the photocurrent was collected and measured via as-synthesised samples (50 μL) over FTO glass substrate in a 0.2 M Na_2SO_4 aqueous solution with -0.8 V potential bias under a 300 W Xe lamp; (D) Electrochemical impedance spectroscopy. a) $\text{g-C}_3\text{N}_4$ bulk; b) CN-SH; c) CN-SPh; d) CN-AP; e) CN-SP samples.

expands the visible-light absorption due to multiple reflections of incident light within the C_3N_4 tube.

It is known that photoluminescence (PL) emission is useful to disclose the efficiency of charge carrier trapping, migration, and transfer, and to understand the fate of electron-hole pairs in semiconductor particles [44]. A broad visible PL band centered at approximately 470 nm is observed for all samples (Fig. 5B), which is attributed to a band-band PL signal with the energy of light approximately equal to the band gap energy of $\text{g-C}_3\text{N}_4$. Doping with phosphorus heteroatoms of $\text{g-C}_3\text{N}_4$, including CN-SH, CN-SPh, CN-AP and CN-SP, possesses weak PL intensity, indicating a much lower recombination rate of photo-induced electrons and holes. The phosphorus doping improves the carrier mobility of $\text{g-C}_3\text{N}_4$, which favours the separation of photo-generated electron-hole pairs and thus decreases the charge carrier recombination rate. Fig. 5C shows the photocurrent responses of $\text{g-C}_3\text{N}_4$ and P-doped samples. We clearly see that the photocurrent value rapidly decreases to zero as soon as the irradiation of light is turned off, and the photocurrent returns to a constant value when the light is turned on. In addition, photocurrent responses do not decay with increase of illuminated time, indicating that prepared catalysts provide a stable quantity of electrons and holes during irradiation. The photocurrent values of P-doped samples are much higher than that of $\text{g-C}_3\text{N}_4$, which are attributed to P-doping and the energy bands.

The results of PL and photocurrent responses indicate high separation and transfer efficiency of photo-generated electron-hole pairs in P-doped samples upon light irradiation [45]. However, the charge transport process, occurring in P-doped samples under dark conditions, which directly reflects its capacity to shuttle and convey charge carriers to the targeted reactive site, is still unknown. Thus, to obtain a deep insight into the charge transport behaviour of P-doped samples in the absence of light excitation, electrochem-

ical impedance spectroscopy (EIS) measurements were carried out under dark conditions. Fig. 5D displays the EIS Nyquist plots of bulk $\text{g-C}_3\text{N}_4$ and P-doped samples, showing a clear decrease in the diameter of the Nyquist plot for all P-doped samples, suggesting a low resistance for interfacial charge transfer from catalysts to reaction molecules.

Suitable band edges for photocatalytic hydrogen evolution make phosphorus modified samples as promising visible-light photocatalysts. The photocatalytic activity was estimated by detecting hydrogen generation from an aqueous solution containing methanol as electron donor under visible light. As shown in Fig. 6a, it is evident that hydrogen evolution rates of the P-doped samples are much higher than that of bulk $\text{g-C}_3\text{N}_4$. Among them, CN-SP exhibits the highest hydrogen evolution rate of $57\text{ }\mu\text{mol h}^{-1}$ (0.1 g catalyst) under visible light irradiation. The highest activity for CN-SP is ascribed to a high ratio P-doping, surface carbon defects, and an enhanced surface area with hierarchical pore structure. A comparison of photocatalytic hydrogen production activities of $\text{g-C}_3\text{N}_4$ and CN-SP is displayed in Fig. 6b. Bulk $\text{g-C}_3\text{N}_4$ only exhibits a very low photocatalytic H_2 production rate of $6\text{ }\mu\text{mol h}^{-1}$. Based on the above analysis, an obvious increase in photocatalytic H_2 production activity is caused by an enlarged surface area, shortened electron-hole transfer distance, and increase of visible-light harvesting.

To analyse the generation of unpaired electrons and holes in the photocatalyst, as-prepared bulk $\text{g-C}_3\text{N}_4$ and CN-SP were measured by ESR spectroscopy at room temperature, as shown in Fig. S7. For bulk $\text{g-C}_3\text{N}_4$ it shows a clear Lorentzian line which is attributed to unpaired electrons on the aromatic rings of C_3N_4 . However, compared with pure $\text{g-C}_3\text{N}_4$, CN-SP possesses much stronger ESR signal for the unpaired electrons, suggesting the presence of carbon defects or P-doping in $\text{g-C}_3\text{N}_4$. Therefore, we conclude that carbon

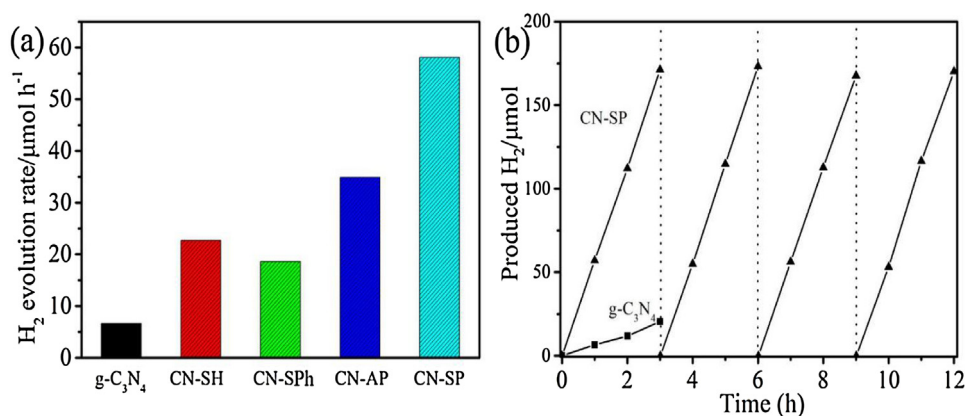


Fig. 6. (a) H₂ evolution rate for g-C₃N₄, CN-SH, CN-SPh, CN-AP and CN-SP samples and (b) time course of H₂ evolution for g-C₃N₄ and CN-SP under visible light irradiation ($\lambda > 420$ nm).

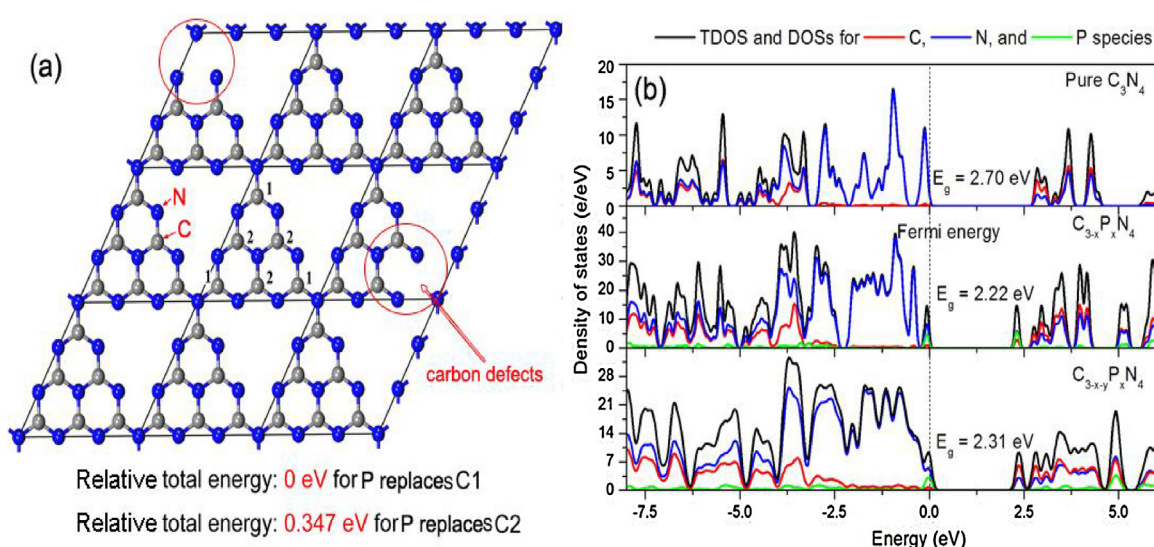


Fig. 7. (a) Relative total energy of P replacing different positions of C, based on g-C₃N₄ theoretical model. (b) Calculated band structures based on density functional theory (DFT) of bulk g-C₃N₄, P-doped g-C₃N₄, and P-doped g-C₃N₄ with carbon defects.

vacancies have successfully formed in g-C₃N₄ after the heat treatment process, which lends support to the XPS results illustrated above. The increase of the unpaired electrons will also improve the efficiency of electron-hole separation of photocatalyst.

The primitive cell of g-C₃N₄ and its PDOSs are shown in Fig. 7(a) and (b), respectively. The computational results suggest that the valence band of g-C₃N₄ located at [−2.0 eV, 0.0 eV] mainly derives from C species, while the conduction band at [3.0 eV, 4.0 eV] originates from C and N species. A band gap of about 2.70 eV is predicted, which is consistent with experimental observations. To reveal the effect of P doping, two possible positions labelled as C1 and C2 in Fig. 7(a) were considered. Our calculation suggests that when P substitutes in the C2 site, the total energy of the system is 0.347 eV higher than that of the other configuration. Therefore, the substitution of C1 by P is more favoured. Because of the doping, PDOSs change significantly, and the conduction band shifts to a lower energy position, leading to a reduction of the band gap from 2.70 to 2.22 eV. This result agrees well with the trend observed in the UV–vis diffuse reflectance spectra above. The origin of the smaller band gap is attributed to the incorporation of P species into the conduction band. Besides the P doping, our calculation also confirms that the appearance of surface carbon defects is also beneficial for

reducing the band gap (2.31 eV) of system. Therefore, we expect that the light absorption range greatly extends, which facilitates the occurrence of photo-generated carriers and improves the photocatalytic performance of materials. The tubular structure of P-doped samples harvests more visible light by P doping and multiple scattering effects, thus yielding more photo-excited electrons.

4. Conclusions

In summary, we present a new strategy, based on phosphorus-containing compounds to prepare precursors for fabrication of novel P-doped g-C₃N₄ tubes with surface carbon defects. The combinative method simultaneously tailors electronic structure, surface defects, active sites, and textural structures to optimize photocatalytic H₂ production. As a result, a strong synergetic enhancement in photocatalytic activity is achieved, and more improved than bulk g-C₃N₄ catalysts. This work provides a simple method for large-scale construction of a new type of g-C₃N₄ nanostructured material for a large variety of catalytic applications.

Acknowledgements

This work was supported by the National Natural Science Foundation of China (51372071, 21571054). Outstanding Subject Leaders Project in Harbin City (2016RAXXJ002).

Appendix A. Supplementary data

Supplementary data associated with this article can be found, in the online version, at <http://dx.doi.org/10.1016/j.apcatb.2017.07.022>.

References

- [1] K. Honda, A. Fujishima, *Nature* 238 (1972) 37–38.
- [2] M. Ni, M.K.H. Leung, D.Y.C. Leung, K. Sumathy, *Renew. Sustain. Energy Rev.* 11 (2007) 401–425.
- [3] X.C. Wang, K. Maeda, A. Thomas, K. Takanabe, G. Xin, J.M. Carlsson, K. Domen, M. Antonietti, *Nat. Mater.* 8 (2009) 76–80.
- [4] A. Melis, T. Happe, *Plant Physiol.* 127 (2011) 740–748.
- [5] F. Li, X. Jiang, J.J. Zhao, S.B. Zhang, *Nano Energy* 16 (2015) 488–515.
- [6] Q.J. Xiang, J.G. Yu, M. Jaroniec, *J. Phys. Chem. C* 115 (2011) 7355–7363.
- [7] Z.W. Zhao, Y.J. Sun, F. Dong, *Nanoscale* 7 (2015) 15–37.
- [8] X.J. Zhu, T.M. Zhang, Z.J. Sun, H.L. Chen, J. Guan, X. Chen, H.X. Ji, P.W. Du, S.F. Yang, *Adv. Mater.* (2017) 1605776.
- [9] X.C. Wang, S. Blechert, M. Antonietti, *ACS Catal.* 2 (2012) 1596–1606.
- [10] S.W. Cao, J.X. Low, J.G. Yu, M. Jaroniec, *Adv. Mater.* 27 (2015) 2150–2176.
- [11] M. Xie, W. Wei, Z.F. Jiang, Y.G. Xu, J.M. Xie, *Ceram. Int.* 42 (2016) 4158–4170.
- [12] H.M. Wang, X.X. Li, J.L. Yang, *ChemPhysChem* 17 (2016) 2100–2104.
- [13] P. Niu, L.L. Zhang, G. Liu, H.M. Cheng, *Adv. Funct. Mater.* 22 (2012) 4763–4770.
- [14] S.E. Guo, Z.P. Deng, M.X. Li, B.J. Jiang, C.G. Tian, Q.J. Pan, H.G. Fu, *Angew. Chem. Int. Ed.* 55 (2016) 1830–1834.
- [15] G. Liu, P. Niu, C.H. Sun, S.C. Smith, Z.G. Chen, G.Q. Lu, H.M. Cheng, *J. Am. Chem. Soc.* 132 (2010) 11642–11648.
- [16] S.C. Yan, Z.S. Li, Z.G. Zou, *Langmuir* 26 (2010) 3894–3901.
- [17] Y. Wang, X.C. Wang, M. Antonietti, *Angew. Chem. Int. Ed.* 51 (2012) 68–89.
- [18] Y. Zheng, J. Liu, J. Liang, M. Jaroniec, S.Z. Qiao, *Energy Environ. Sci.* 5 (2012) 6717–6731.
- [19] P. Wu, J.R. Wang, J. Zhao, L.J. Guo, F.E. Osterloh, *J. Mater. Chem. A* 2 (2014) 20338–20344.
- [20] Q.H. Liang, Z. Li, Z.H. Huang, F.Y. Kang, Q.H. Yang, *Adv. Funct. Mater.* 25 (2015) 6885–6892.
- [21] P. Niu, G. Liu, H.M. Cheng, *J. Phys. Chem. C* 116 (2012) 11013–11018.
- [22] Q.L. Tay, P. Kanhere, C.F. Ng, S. Chen, S. Chakraborty, A.C.H. Huan, T.C. Sum, R.v. Ahuja, Z. Chen, *Chem. Mater.* 27 (2015) 4930–4933.
- [23] P.S. Corbin, S.C. Zimmerman, P.A. Thiessen, N.A. Hawryluk, T.J. Murray, *J. Am. Chem. Soc.* 123 (2001) 10475–10488.
- [24] L.J. Prins, F.D. Jong, P. Timmerman, D.N. Reinhoudt, *Nature* 408 (2000) 181–184.
- [25] G.H. Dong, K. Zhao, L.Z. Zhang, *Chem. Commun.* 48 (2012) 6178–6180.
- [26] J. Sehnert, K. Baerwinkel, J. Senker, *J. Phys. Chem. B* 111 (2007) 10671–10680.
- [27] Y.S. Jun, E.Z. Lee, X.C. Wang, W.H. Hong, G.D. Stucky, A. Thomas, *Adv. Funct. Mater.* 23 (2013) 3661–3667.
- [28] Y.J. Zhou, L.X. Zhang, J.J. Liu, X.Q. Fan, B.Z. Wang, M. Wang, W.C. Ren, J. Wang, M.L. Li, J.L. Shi, *J. Mater. Chem. A* 3 (2015) 3862–3867.
- [29] Y.J. Zhang, T. Mori, J.H. Ye, M. Antonietti, *J. Am. Chem. Soc.* 132 (2010) 6294–6295.
- [30] Y.P. Zhu, T.Z. Ren, Z.Y. Yuan, *ACS Appl. Mater. Interfaces* 7 (2015) 16850–16856.
- [31] L.G. Zhang, X.F. Chen, J. Guan, Y.J. Jiang, T.G. Hou, X.D. Miao, *Mater. Res. Bull.* 48 (2013) 3485–3491.
- [32] Z.F. Hu, Z.R. Shen, J.C. Yu, *Green Chem.* 19 (2017) 588–613.
- [33] S.Z. Hu, L. Ma, J.G. You, F.Y. Li, Z.P. Fan, F. Wang, D. Liu, J.Z. Gui, *RSC Adv.* 4 (2014) 21657–21663.
- [34] F.X. Cheng, J. Yan, C.J. Zhou, B.H. Chen, P.R. Li, Z. Chen, X.P. Dong, *J. Colloid Interface Sci.* 468 (2016) 103–109.
- [35] J.S. Zhang, X.F. Chen, K. Takanabe, K. Maeda, K. Domen, J.D. Epping, X.Z. Fu, M. Antonietti, X.C. Wang, *Angew. Chem. Int. Ed.* 49 (2010) 441–444.
- [36] G.G. Zhang, J.S. Zhang, M.W. Zhang, X.C. Wang, *J. Mater. Chem.* 22 (2012) 8083–8091.
- [37] X.F. Li, J. Zhang, L.H. Shen, Y.M. Ma, W.W. Lei, Q.L. Cui, G.T. Zou, *Appl. Phys. A* 94 (2009) 387–392.
- [38] Y.G. Xu, H. Xu, L. Wang, J. Yan, H.M. Li, Y.H. Song, L.Y. Huang, G.B. Cai, *Dalton Trans.* 42 (2013) 7604–7613.
- [39] G.Q. Li, N. Yang, W.L. Wang, W.F. Zhang, *J. Phys. Chem. C* 113 (2009) 14829–14833.
- [40] F. Dong, Z.W. Zhao, T. Xiong, Z.L. Ni, W.D. Zhang, Y.J. Sun, W.K. Ho, *Appl. Mater. Interfaces* 5 (2013) 11392–11401.
- [41] H.J. Yan, Y. Chen, S.M. Xu, *Int. J. Hydrogen Energy* 37 (2012) 125–133.
- [42] Y.J. Zhou, L.X. Zhang, J.J. Liu, X.Q. Fan, B.Z. Wang, M. Wang, W.C. Ren, J. Wang, M.L. Li, J.L. Shi, *J. Mater. Chem. A* 3 (2015) 3862–3867.
- [43] L. Yang, B. Kruse, *J. Opt. Soc. Am. A* 21 (2004) 1933–1941.
- [44] J.W. Fang, H.Q. Fan, M.M. Li, C.B. Long, *J. Mater. Chem. A* 3 (2015) 13819–13826.
- [45] B. Chai, J.T. Yan, C.L. Wang, Z.D. Ren, Y.C. Zhu, *Appl. Surf. Sci.* 391 (2017) 376–383.